

Volumetric fault image enhancement — Some applications

Satinder Chopra¹ and Kurt J. Marfurt²

Abstract

The interpretation of faults on 3D seismic data is often aided by the use of geometric attributes such as coherence and curvature. Unfortunately, these same attributes also delineate stratigraphic boundaries (geologic signal) and apparent discontinuities due to cross-cutting seismic noise. Effective fault mapping thus requires enhancing piecewise continuous faults and suppressing stratabound edges and unconformities as well as seismic noise. To achieve this objective, we apply two passes of edge-preserving structure-oriented filtering followed by a recently developed fault enhancement algorithm based on a directional Laplacian of a Gaussian operator. We determine the effectiveness of this workflow on a 3D seismic volume from central British Columbia, Canada.

Introduction

Coherence and curvature are iconic attributes now commonly available on most interpretation workstations that help characterize small- and large-scale faults, large fractures, fault truncations, pinch-outs, buried channels, reef edges, and unconformities. Various algorithms are available for coherence computation including the crosscorrelation (Bahorich and Farmer, 1995), semblance (Marfurt et al., 1998), geometric structure tensor (Bakker, 2003), eigendecomposition (Gersztenkorn and Marfurt, 1999), and energy-ratio (Chopra and Marfurt, 2008) methods. Each one of these methods has advantages and limitations in terms of the quality of the coherence imaging of the features of interest and the run times associated with them. Similarly, multi-spectral most-positive and most-negative curvatures (Chopra and Marfurt, 2007) are commonly used to characterize folding, faulting, differential compaction, dissolution, and fault zones that fall below the seismic resolution. Due to operator aliasing, acquisition footprint, and other noise, almost all coherence and curvature volumes computed from 3D land surveys benefit by appropriate data conditioning. Such data conditioning may include the reduction of cross-cutting and random noise, sharpening or enhancement of discontinuities, spectral balancing, and/or interpolation of missing data (Chopra and Marfurt, 2013), and more.

Second derivative Laplacian of a Gaussian (LoG) filters have long been used in photographic edge enhancement. To enhance lateral structural and stratigraphic discontinuities in 3D seismic data, Chopra and Marfurt (2007) apply a 2D LoG filter oriented along a structural

dip. Geologic features comprising channels and fault trends seen on the sharpened coherence displays are crisper and easier to interpret than they are on the equivalent coherence displays. Although coherence anomalies associated with unconformities are partially suppressed, the structure-oriented LoG does not merge previously disjointed fault segments seen on vertical slices.

Considerable effort has been invested in the enhancement of faults seen in geometric attributes. Dorn and Kadlec (2011) describe a fault enhancement approach that generates measures of fault dip, fault azimuth, and probability that a fault exists at each voxel. Using an eigenstructure analysis of covariance matrices computed from a window of amplitude gradient vectors, Lavalie et al. (2007) introduce a nonlinear filtering technique for fault enhancement followed by subsequent fault object extraction. Barnes (2006) computes eigenvectors of windowed coherence values to design directional filters that first dilate and then skeletonize discontinuities, generating preconditioned volumes for subsequent fault extraction.

Machado et al. (2016) build on Barnes' (2006) algorithm and compute eigenvectors of the second moment tensor computed from a window of coherence (or curvature) values. They then apply a directional LoG filter perpendicular to locally planar attribute anomalies, smoothed parallel to the planar events, and apply a muting filter to suppress planar events subparallel to the reflector dip.

In this paper, we discuss the enhancement of faults and the axial planes of folds by preconditioning of the seismic data followed by directional smoothing and

¹Arcis Seismic Solutions, TGS, Calgary, Canada. E-mail: schopra@arcis.com.

²The University of Oklahoma, Norman, Oklahoma, USA. E-mail: kmarfurt@ou.edu.

Manuscript received by the Editor 4 August 2016; revised manuscript received 7 November 2016; published online 6 February 2017. This paper appears in *Interpretation*, Vol. 5, No. 2 (May 2017); p. T151–T161, 14 FIGS.

<http://dx.doi.org/10.1190/INT-2016-0129.1>. © 2017 Society of Exploration Geophysicists and American Association of Petroleum Geologists. All rights reserved.

edge enhancement, thereby enhancing geologic features of interest for more effective interpretation.

Preconditioning with structure-oriented filtering

The objective in preconditioning seismic data is to suppress noise and to improve the lateral and vertical resolution of the signal to improve (or facilitate) subsequent amplitude and/or attribute analysis.

The application of mean and median filters to seismic data that have significant dips, faults, and stratigraphic boundaries may not be adequate and may result in artifacts such as smeared edges and decreased

resolution. [Hoecker and Fehmers \(2002\)](#) and [Luo et al. \(2002\)](#) introduce alternative “structure-oriented” filtering workflows that smooth the data along the structural dip while at the same time preserving edges. Both algorithms require first computing the structural dip. In [Hoecker and Fehmers \(2002\)](#) algorithm, one also pre-computes the location of major discontinuities using chaos, a by-product of their dip calculation. [Luo et al. \(2002\)](#) algorithm uses a [Kuwahara et al. \(1976\)](#) filter construct, whereby the edges are preserved by searching for and selecting the most homogeneous (lowest standard deviation) patch of data around each sample

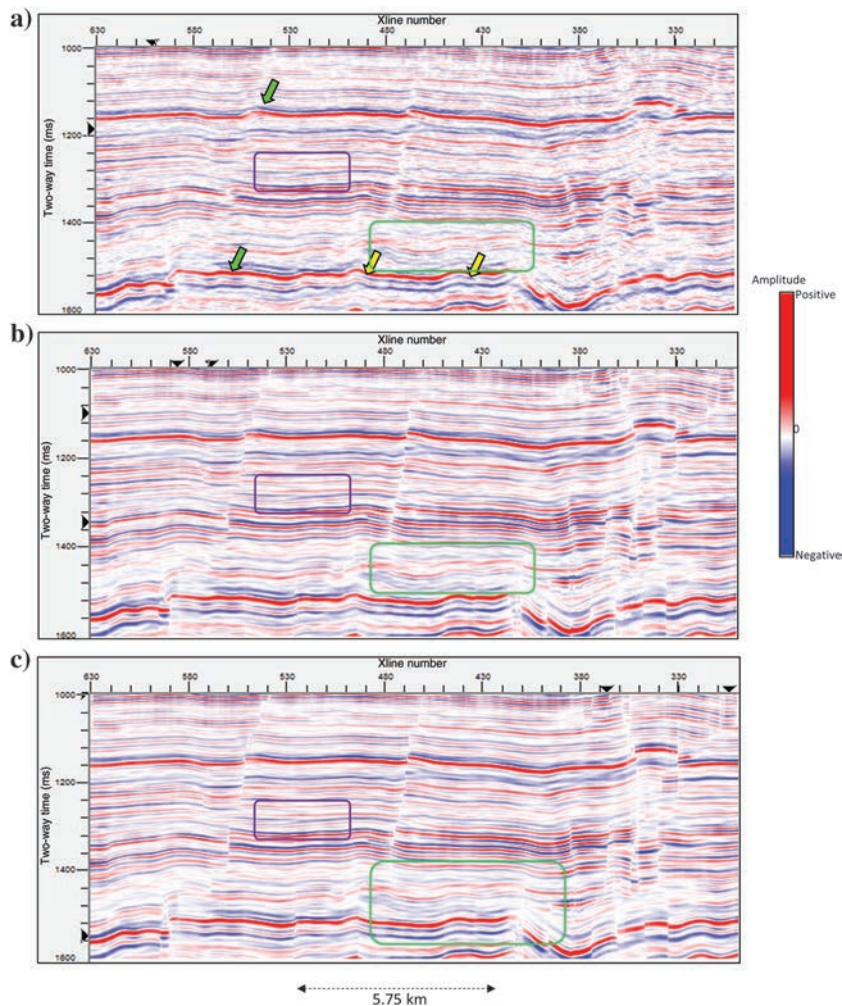


Figure 1. Vertical slices through the seismic amplitude volume (a) before and after (b) one pass and (c) two passes of Kuwahara principal component structure-oriented filtering. Notice how cross-cutting noise inconsistent with structural dip is suppressed, amplitudes consistent with structural dip are preserved, whereas discontinuities are sharpened with each iteration of filtering. The green arrows indicate the footwall of a fault, whereas the yellow arrows indicate folds that may be associated with pop-up features. The purple box indicates an area exhibiting a low amplitude but low S/N that will give rise to coherence artifacts parallel to stratigraphy. The green box indicates an area exhibiting angular higher amplitude and higher S/N angular unconformities that will give rise to coherence signal parallel to stratigraphy. The size of the structure-oriented filter analysis window is five traces by 11 2 ms samples (data courtesy of Arcis Seismic Solutions, TGS, Calgary).

in the seismic volume. The output filtered data are then the average value (mean) of the selected patch ([AlBinHasan et al., 2006](#)). [Marfurt \(2006\)](#) modifies this latter approach, using overlapping windows to determine the best window to use for subsequent, mean, alpha-trimmed mean, or Karhunen-Loève (KL) filtering. Although the KL filter is a linear filter, the Kuwahara process is not, such that not only the lateral resolution but also the temporal resolution can be increased (or sharpened) about the fault edges ([Hutchinson, 2016](#)). Practical applications of Kuwahara filtering on real seismic data can be found in [Marfurt \(2006\)](#) and [Chopra and Marfurt \(2008\)](#).

In [Figure 1a](#), we show a vertical slice through a 3D seismic amplitude volume from central British Columbia, Canada. These data were subjected to two passes of structure-oriented filtering with Kuwahara sharpening, as shown in [Figure 1b](#) and [1c](#). Notice the crisp definition of the faults and the higher signal-to-noise ratio (S/N) of the filtered amplitude data. The second pass of filtering ([Figure 1c](#)) has resulted in greater sharpening of the discontinuities. A third pass results in little change, indicating that the algorithm has converged. Attribute computation carried out on such data with sharpened discontinuities is likely to (i.e., “preconditioned” to) produce superior results.

In [Figure 2](#), we show a cartoon that illustrates the value of the iterative application of small structure-oriented filters versus a single, larger analysis window encompassing the same number of traces. The figure shows a 2D mean filter that tracks the reflector dip better, and its iterative application with tapered filter weights performs much better on the input seismic data.

Directional LoG filter

Barnes (2006) introduces a discontinuity enhancement filter that, when applied to coherence volumes, results in more continuous skeletonized fault surfaces. Although the computation of the fault orientation is clearly described, details of the subsequent fault dilation and skeletonization are not. Machado et al. (2016) build on Barnes' (2006) fault orientation analysis and describe a workflow to compute the "fault" dip magnitude, "fault" dip azimuth, and fault probability at each voxel using a discontinuity (coherence/curvature) volume as well as the inline and crossline dip/azimuth attributes.

Their approach consists of constructing a second-order moment tensor of a discontinuity attribute α_m within an M -voxel analysis window:

$$C_{ij} = \frac{\sum_{m=1}^M x_{im}x_{jm}\alpha_m}{\sum_{m=1}^M \alpha_m}, \quad (1)$$

where the variables x_{im} and x_{jm} are the distances from the center of the analysis window along axis $i = 1, 2, 3$ and $j = 1, 2, 3$ of the m th data point.

In general, in the absence of any feature of interest, the value of α_m should be zero, as would be seen for high-coherence data. For such data, the maximum coherence coefficient is unity ($c_m = 1$) and α_m is defined as $\alpha_m = 1 - c_m$. For 3D seismic data, the second moment tensor \mathbf{C} has three eigenvalues λ_j and eigenvectors \mathbf{v}_j , governed by $\lambda_1 \geq \lambda_2 \geq \lambda_3$.

If $\lambda_1 \approx \lambda_2 \gg \lambda_3$, the discontinuity attribute defines a plane that is normal to the third eigenvector \mathbf{v}_3 .

If $\lambda_1 \approx \lambda_2 \approx \lambda_3$, then the discontinuity attribute exhibits no preferred orientation but instead represents either chaotic (large λ_3) or homogeneous seismic facies (small λ_3).

The choice of the size of the analysis window M has a bearing on the resulting eigenvalues and eigenvectors. The eigenvectors \mathbf{v}_1 and \mathbf{v}_3 define a plane that fits the cloud of points, in a least-squares sense. So as not to bias the estimates along any axis, the data are converted to depth using an appropriate conversion velocity, which enables the definition of a spherical window. In that case, \mathbf{v}_3 is perpendicular to the hypothesized fault.

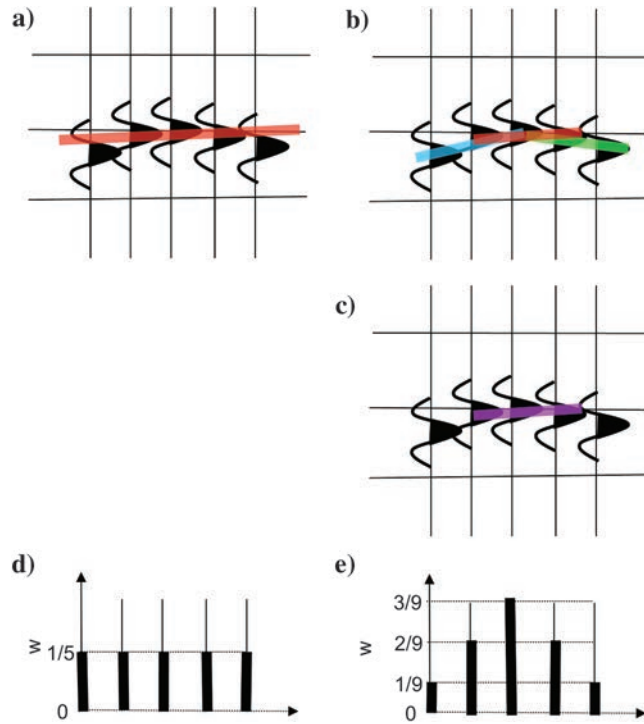


Figure 2. A cartoon showing the value of iterative application of small structure-oriented filters versus a single, larger analysis window encompassing the same number of traces. For simplicity, this cartoon shows a 2D mean filter. There are three advantages of the iterative filter: First, the three smaller filters in panel (b) better track the reflector dip than the single larger filter in panel (a). Second, the smaller filters are applied (c) iteratively, which is equivalent to convolving the filter coefficients. (d) The filter coefficients in panels (a) have equal weights of $1/5$. (e) The filter weights in panels (b and c) are $1/3$, but when convolved give tapered filtered weights of $(1/9, 2/9, 3/9, 2/9, 1/9)$. Third, the cost of n iterations of a 3×3 trace filter is $n \times 3 \times 3 = 9n$, whereas that of a single $3n \times 3n$ filter is a more computationally intensive $9n^2$.

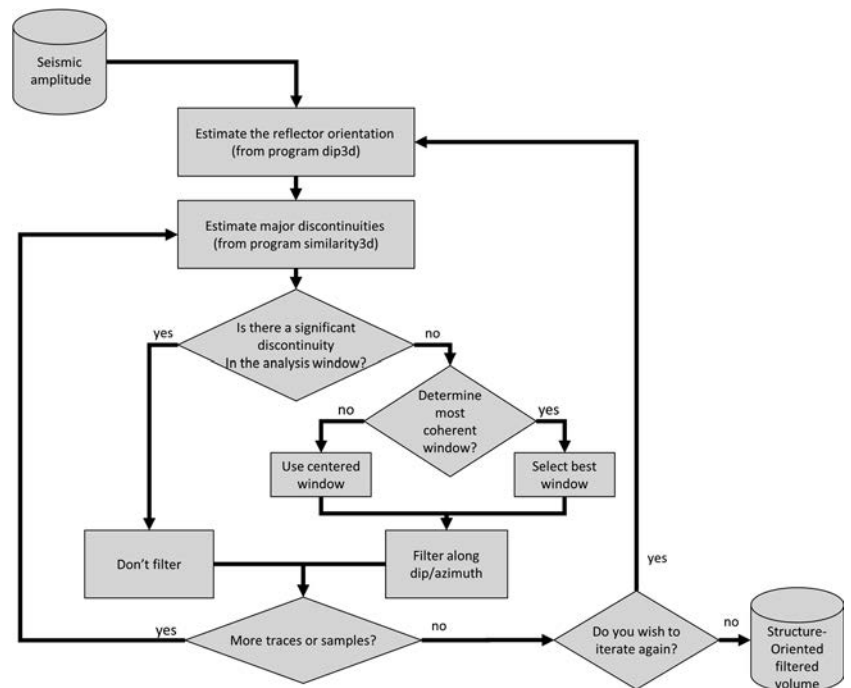


Figure 3. Workflow for structure-oriented filtering.

To display the orientation of a planar feature, Machado et al. (2016) define the “fault” dip magnitude θ and the “fault” dip azimuth ψ as follows:

$$\theta = \text{ACOS}(v_{33}), \quad (2)$$

$$\psi = \text{ATAN2}(v_{32}v_{31}), \quad (3)$$

where the components of the eigenvector \mathbf{v}_3 are defined as

$$\mathbf{v}_3 = \hat{\mathbf{x}}_1 v_{31} + \hat{\mathbf{x}}_2 v_{32} + \hat{\mathbf{x}}_3 v_{33}, \quad (4)$$

where the x_1 axis is oriented positive to the north, the x_2 axis is oriented positive to the east, and the x_3 axis is oriented positive downward. The term “fault” has been put in quotes because the algorithm can also be used to enhance axial planes (from curvature input) and unconformities (from coherence or reflector convergence input).

The classic LoG filter smooths and sharpens in all three directions and has the general form:

$$\begin{aligned} (\text{LG})\alpha = \sum_{m=1}^M \left\{ -\frac{1}{\sigma_1^2} + \frac{x_{1m}^2}{2\sigma_1^4} - \frac{1}{\sigma_2^2} + \frac{x_{2m}^2}{2\sigma_2^4} \right. \\ \left. - \frac{1}{\sigma_3^2} + \frac{x_{3m}^2}{2\sigma_3^4} \right\} \exp \left[-\left(\frac{x_{1m}^2}{2\sigma_1^2} + \frac{x_{2m}^2}{2\sigma_2^2} \right. \right. \\ \left. \left. + \frac{x_{3m}^2}{2\sigma_3^2} \right) \right] \alpha_m, \end{aligned} \quad (5)$$

where σ_j^2 defines the variance of the Gaussian smoother along the j th axis.

Because we wish to sharpen perpendicular to the hypothesized fault (along eigenvector \mathbf{v}_3) and smooth parallel to the fault (along eigenvectors \mathbf{v}_1 and \mathbf{v}_2), we must first rotate our natural (east, north, vertical) x -coordinate system, to a ξ -coordinate system aligned with the ξ_3 axis, defined as the eigenvector \mathbf{v}_3 in the natural x -coordinate system,

$$\xi = \mathbf{R}\mathbf{x}, \quad (6)$$

where \mathbf{R} is the rotation matrix given explicitly by

$$\begin{pmatrix} \xi_1 \\ \xi_2 \\ \xi_3 \end{pmatrix} = \begin{pmatrix} v_{11} & v_{12} & v_{13} \\ v_{21} & v_{22} & v_{23} \\ v_{31} & v_{32} & v_{33} \end{pmatrix} \begin{pmatrix} x_1 \\ x_2 \\ x_3 \end{pmatrix}. \quad (7)$$

Because we want to smooth along the faults, we set $\sigma_3^2 < \sigma_1^2 = \sigma_2^2$.

Finally, we wish to modify the LoG operator to be directional: sharpening only along the direction perpendicular to the planar discontinuity (along the ξ_3 axis):

$$\begin{aligned} \left(\frac{\partial^2 \mathbf{G}}{\partial \xi^2} \right) \alpha = \sum_{m=1}^M \left\{ -\frac{1}{\sigma_3^2} + \frac{\xi_{3m}^2}{\sigma_3^4} \right\} \\ \times \exp \left[-\left(\frac{\xi_{1m}^2}{2\sigma_1^2} + \frac{\xi_{2m}^2}{2\sigma_2^2} + \frac{\xi_{3m}^2}{2\sigma_3^2} \right) \right] \alpha_m. \end{aligned} \quad (8)$$

The directional LoG filter enhances all planar events, regardless of their orientation. Coherence will often delineate stratigraphic features, such as onlap, downlap, toplap, and erosional unconformities that we may not wish to include in a “fault enhancement” workflow. Because we know the normal to the reflector \mathbf{n}_r and the normal to the planar event \mathbf{v}_3 , we can construct a Tukey filter to suppress such stratigraphic anomalies (Figure 3). Alternatively, if we wished to enhance such stratigraphic features, we would construct a Tukey filter to suppress the steeply dipping faults. Note that there is no way to differentiate faults that

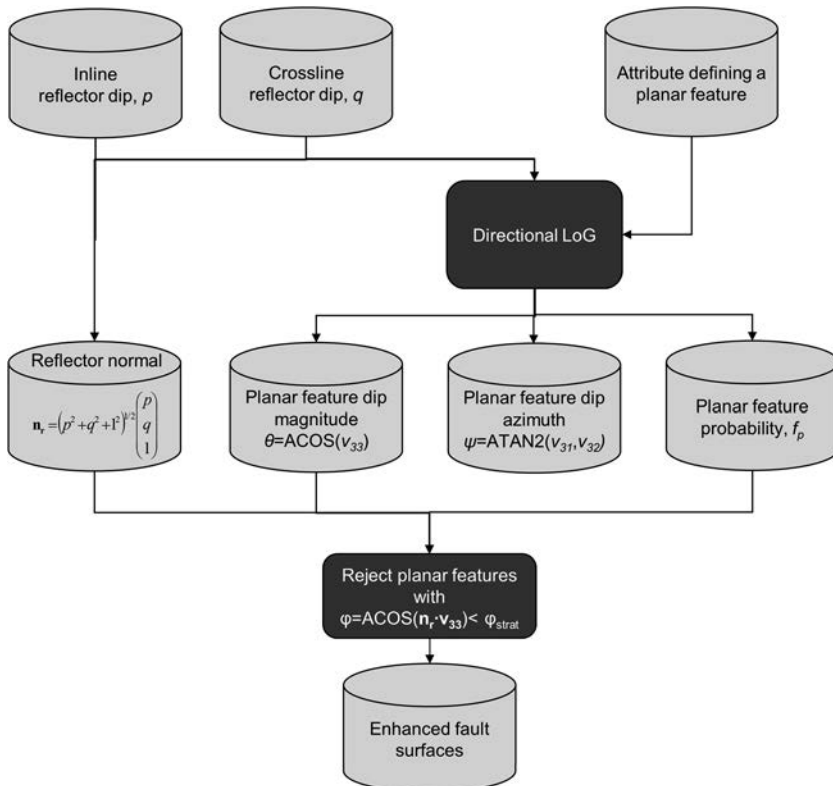


Figure 4. Block diagram illustrating the workflow followed for volumetric fault image enhancement. In our application, we chose $\phi_{\text{strat}} = 20^\circ$, such that any stratigraphic discontinuities parallel to the reflector dip and any faults that sole out into the reflectors are suppressed.

have soled out into the reflector from stratigraphic events.

Figure 3 shows the workflow for structure-oriented filtering wherein the reflector dip and discontinuities are first estimated within the analysis window. When it comes to filtering of noise, care is taken not to smooth across discontinuities and thus smear them.

Application

All applications are computed on analytic (often called complex) traces defined as $d + id^H$, where d is the measured trace, d^H is its Hilbert transform (or quadrature), and $i = (-1)^{1/2}$. Using the analytic trace reduces artifacts encountered when using small analysis windows about zero crossings in the measured data (Chopra and Marfurt, 2007). Following the workflow in Figure 4, we construct volumetric estimates of the reflector dip using a semblance-driven search algorithm described by Marfurt (2006). Next, we compute coherence along the structure using an energy-ratio algorithm (Chopra and Marfurt, 2008), which computes the ratio of the energy of the coherent component of the analytic trace to the energy of the original analytic trace. We compute the coherent component of the analytic trace by projecting the original data onto the first eigenvector of the covariance matrix (the same process used in KL filtering). The volumetric estimates of principal curvature are generated by computing the derivatives of the volumetric reflector dip components providing a full 3D volume of the curvature values. Moreover, the curvature operator is filtered in the wavenumber domain, resulting in low-pass (long-wavelength) and broader band (short-wavelength) principal curvature results (Al-Dossary and Marfurt, 2006; Chopra and Marfurt, 2010). The “long-wavelength” and the “short-wavelength” versions of the curvature provide different levels of detail and are useful in appropriate applications. In Figure 5, we show equivalent segments of the same seismic section shown in Figure 1 from the coherence and curvature attributes computed on input seismic data, without any preconditioning. The discontinuities seen on the vertical seismic section are now seen as well-defined lineaments on the attribute displays.

We now put the coherence through the workflow described above for the computation of the “fault” dip magnitude, the “fault” dip azimuth, and the fault prob-

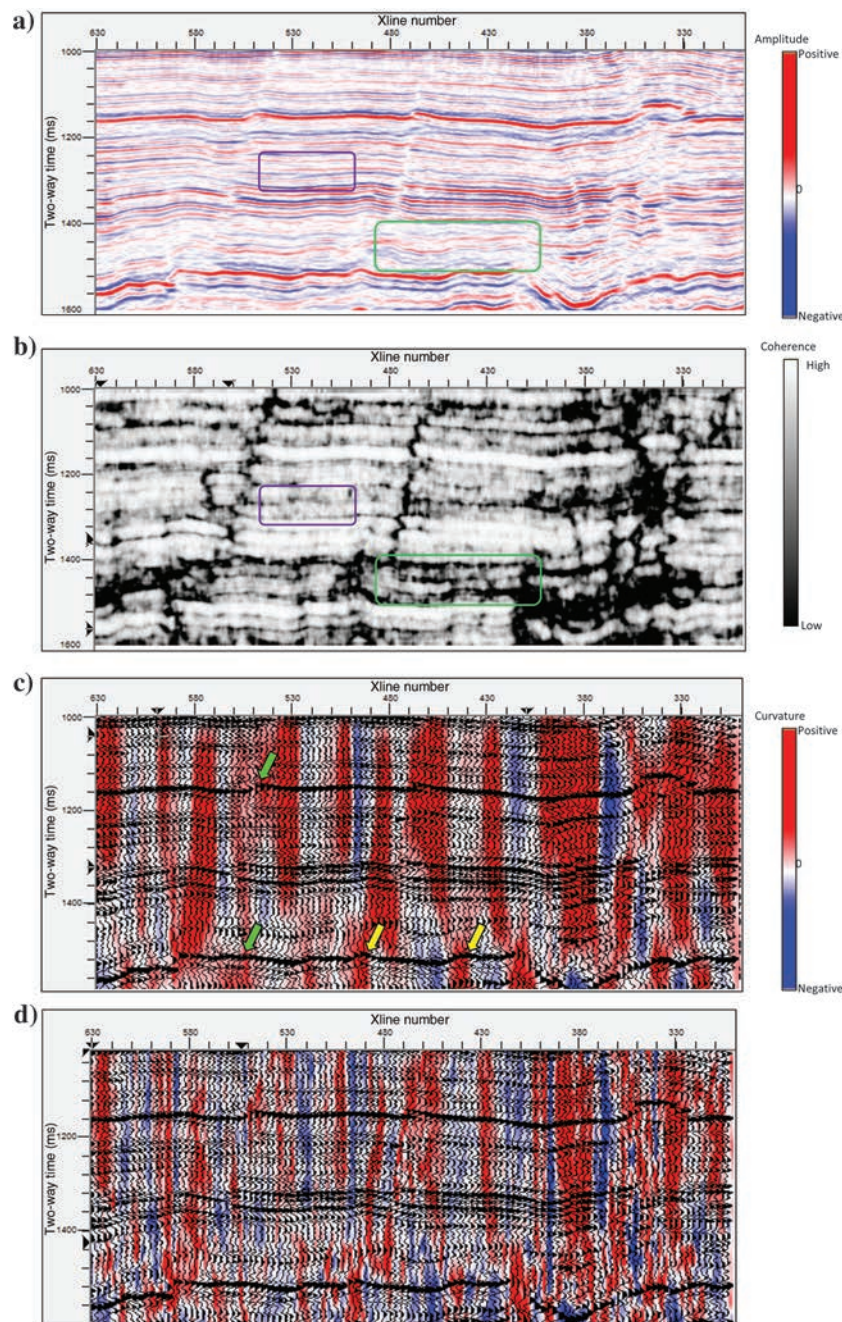


Figure 5. (a) The same vertical slice through the seismic amplitude volume shown in Figure 1a (before data conditioning) with corresponding vertical slices through (b) coherence, (c) most-positive long-wavelength curvature, and (d) most-positive short-wavelength curvature. In panels (c and d), every third seismic trace from the input seismic data volume is overlaid in wiggle/variable area to accurately correlate the seismic signatures with the attributes displayed in variable density in the background. Fault discontinuities appear as vertical lineaments in coherence and curvature. Coherence also exhibits low values parallel to the structure, some of which correlate to unconformities, and others that correlate to areas of low S/N. Although curvature delineates the anticlinal shaped footwall edge of faults (green arrows), it also delineates anticlinal folds (yellow arrow) that may be pop-up features (data courtesy of Arcis Seismic Solutions, TGS, Calgary).

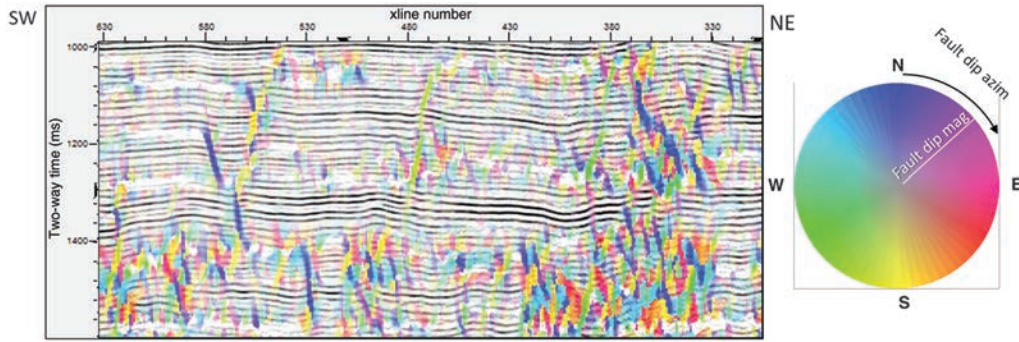


Figure 6. Corendered fault dip azimuth, fault dip magnitude, fault probability, and seismic amplitude. Faults dipping to the north appear as blue, whereas those dipping toward the south appear as yellow (data courtesy of Arcis Seismic Solutions, TGS, Calgary).

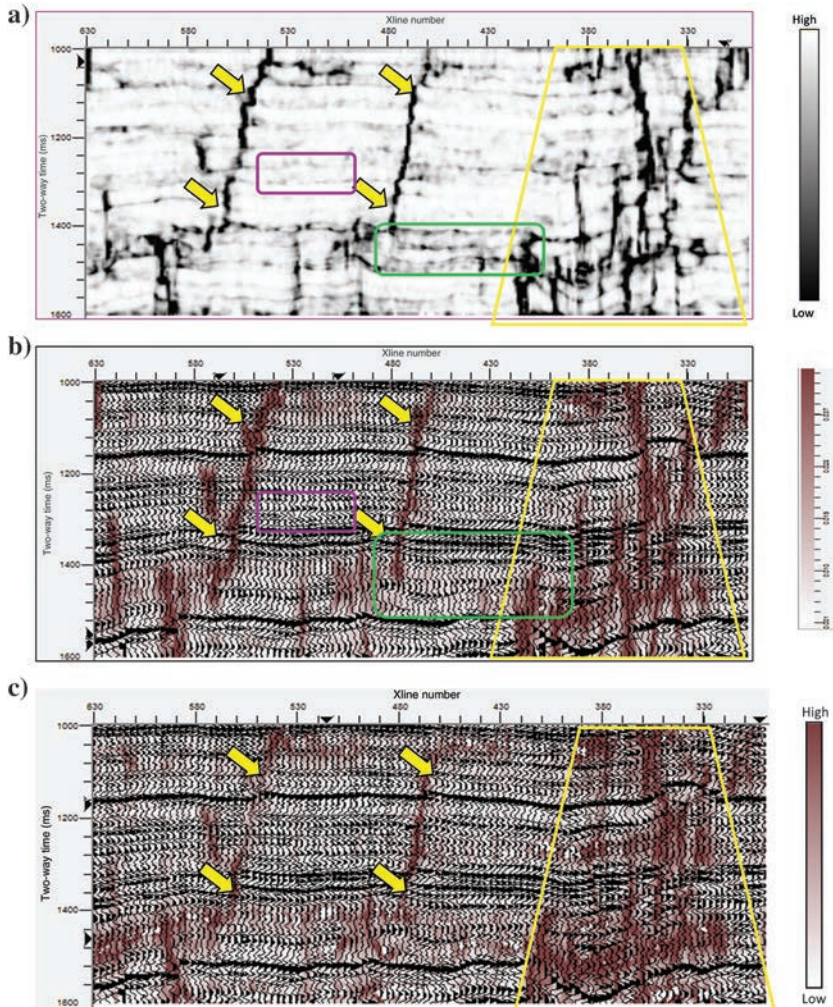


Figure 7. Vertical slices computed from the data volume shown in Figure 1b (after one pass of Kuwahara principal component structure-oriented filtering) through (a) coherence and (b) subsequent computation of fault probability. Notice that discontinuities subparallel to the reflector dip have been suppressed, whereas the previously disjointed faults (yellow arrows) are now more continuous. Smaller faults within the yellow trapezoid are also better defined than those seen in Figure 5b. Every third seismic trace from the input seismic data volume is overlaid to accurately correlate the seismic signatures with the fault probability attribute shown in panel (b) (data courtesy of Arcis Seismic Solutions, TGS, Calgary).

ability volumes that are generated from the coherence attribute as well as the inline and the crossline components of the dip attributes. In Figure 6, we show the corendered fault dip azimuth, fault dip magnitude, fault probability, and seismic amplitude. Faults dipping to the north appear as blue, whereas those dipping toward the south appear as yellow.

Encouraged with these results, we repeat the above fault image enhancement workflow on the input seismic data that has been put through one pass of structure-oriented filtering with Kuwahara sharpening shown in Figure 1b. We show the resultant equivalent sections from the coherence and the fault probability volumes in Figure 7, and we notice that not only are the prominent fault probability lineaments imaged and aligned with the fault discontinuities (yellow arrows) much better, but also the smaller ones in the yellow highlighted area are better defined as well.

We again repeat the above steps with the input seismic data that were put through two passes of structure-oriented filtering with Kuwahara filtering. The results are shown in Figure 8. The prominent fault probability lineaments as well as the smaller ones are now imaged much better and can be a good aid for interpretation of faults or even as an input for the automatic generation of fault planes.

Although the vertical displays shown in the earlier figures convey the value addition in terms of smoothing and crisp definition of the fault lineaments, in Figure 9 we exhibit time slices at $t = 1300$ ms from the energy-ratio coherence attribute as run on the input seismic data (Figure 9a), and then the same data after one pass (Figure 9b) and two

passes (Figure 9c) of structure-oriented filtering with Kuwahara sharpening. The equivalent displays from fault probability are shown in Figure 10. We qualify this conclusion with the addition of 3D volume visuali-

zation and correlation of the fault probability volume with 3D seismic data in Figure 11a, and their corendering in Figure 11b. Such fault-enhanced visualization facilitates their interpretation.

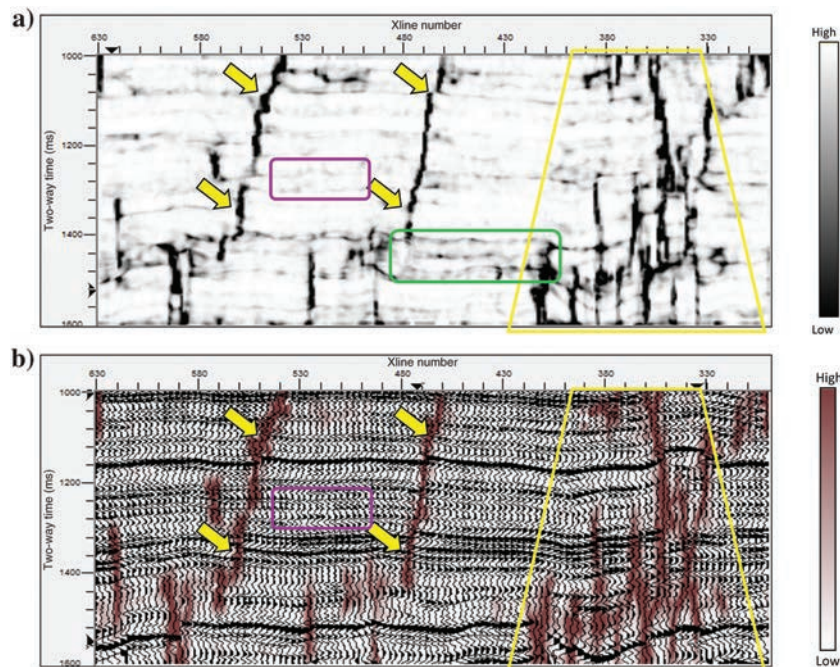


Figure 8. Vertical slices computed from the data volume shown in Figure 1c (after two passes of Kuwahara principal component structure-oriented filtering) through (a) coherence and (b) subsequent computation of fault probability. Note further improvements in fault resolution and continuity. Also note that the stratigraphic artifacts in the purple box are suppressed after two passes of SOF, whereas the stratigraphic angular unconformity in the green box is preserved. This latter feature is suppressed by using the Tukey filter described in Figure 3 (data courtesy: Arcis Seismic Solutions, TGS, Calgary).

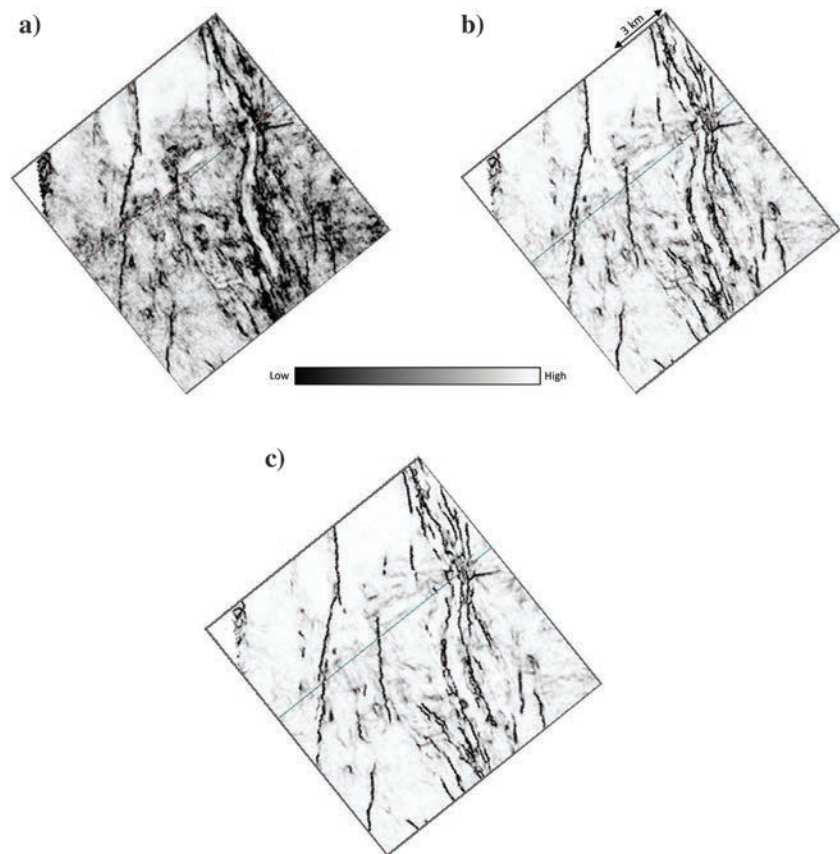


Figure 9. Time slices at $t = 1300$ ms through coherence volumes generated from the 3D seismic amplitude volume (a) before and after (b) one pass and (c) two passes of Kuwahara principal component structure-oriented filtering. Notice how the S/N and the sharpening of the discontinuities improves with each pass of filtering. The line across each of the displays is the location of the section shown in the other displays (data courtesy of Arcis Seismic Solutions, TGS, Calgary).

The fault probability volumes discussed above were all generated from the coherence attributes being used as the attribute defining the fault/axial plane as illustrated in the workflow diagram shown in Figure 4. We repeated the last step, i.e., the generation of fault probability, not from the coherence attribute, but from the short-wavelength version of most-positive curvature. A section from this data, equivalent to the sections shown in the previous figures, is shown in Figure 12a. In Figure 12b, we show the equivalent fault probability section derived therefrom. Notice that there are many

similarities, as seen by the lineaments indicated with the yellow arrows and the highlighted area, but at the same time there are subtle differences that we need to be mindful about. Such differences are indicated with cyan arrows.

Figure 13 shows equivalent time slices through fault probability volumes generated from coherence (Figure 13a) and curvature (Figure 13b). While the lineaments seen in Figure 12a are crisp and more coherent, there are more detailed lineaments seen in Figure 13b, but they are less coherent. We track some of the linea-

Figure 10. Time slices at $t = 1300$ ms through fault probability volumes computed from the three coherence volume shown in Figure 8: (a) without and (b) with one and (c) with two passes of Kuwahara principal component structure-oriented filtering. Discontinuities subparallel to the reflector dip have been suppressed. Note the improved continuity and extent of the faults in which the fault enhancement algorithm has joined previously disjoint fault segments. The line across each of the displays is the location of the section shown in the other displays (data courtesy of Arcis Seismic Solutions, TGS, Calgary).

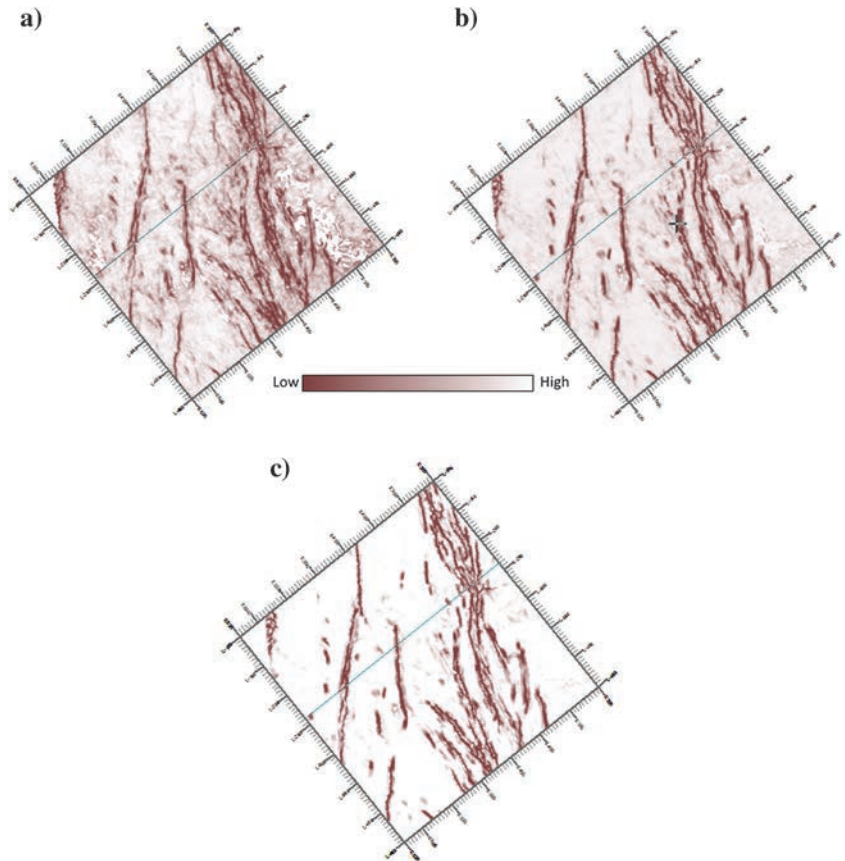
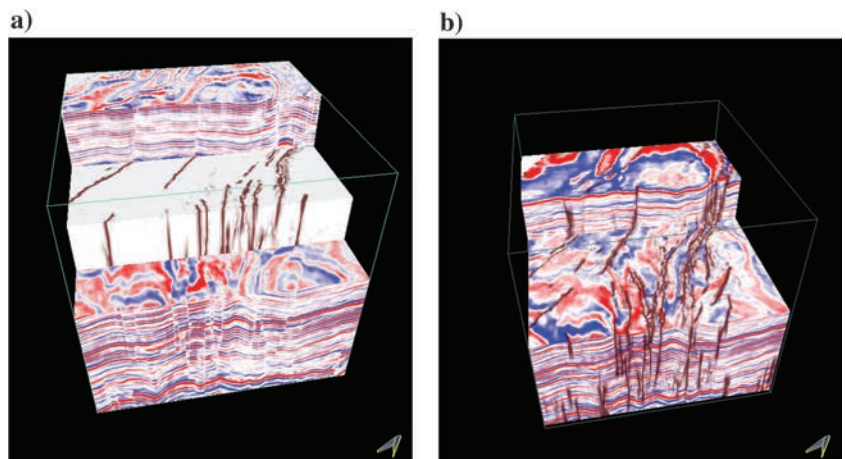


Figure 11. (a) The seismic volume after two passes of Kuwahara principle component structure-oriented filtering with an inset cube of the fault probability volume and (b) the two volumes corendered. These examples illustrate a useful way of carrying out fault interpretation (data courtesy of Arcis Seismic Solutions, TGS, Calgary).



ments on the coherence-derived fault probability display (Figure 14a) in different colors and overlay them on the curvature-derived fault probability display (Figure 14b).

If we recollect the differences in the interpretation of the lineaments from the coherence and the equivalent most-positive or most-negative curvature displays, it is

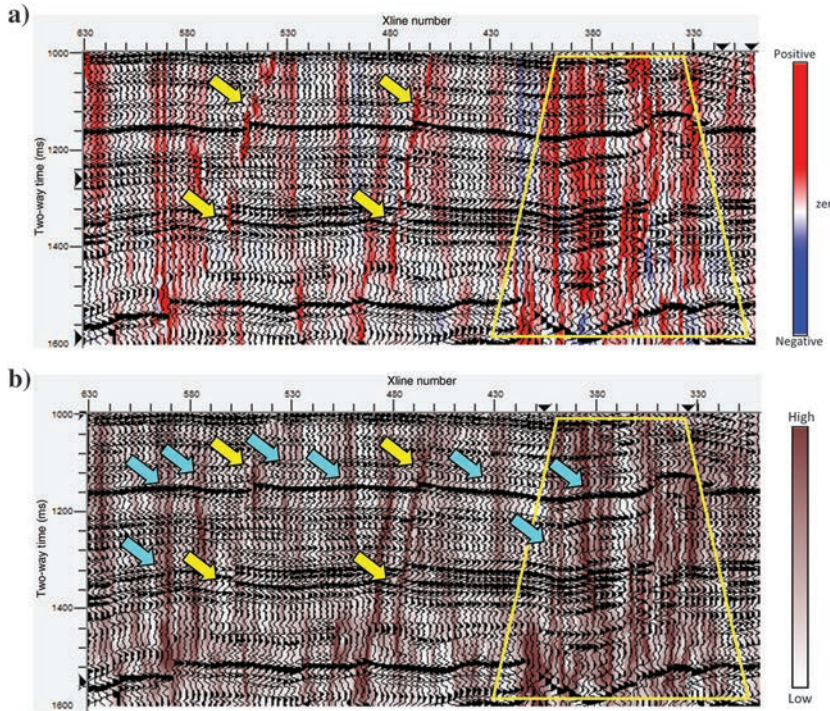


Figure 12. The same vertical slice shown in previous figures but now through the (a) short wavelength most-positive curvature volume computed from the seismic amplitude volume after two passes of Kuwahara principal component structure-oriented filtering and (b) a subsequent “fault” probability volume computed from the most-positive curvature volume. In most cases, the most-positive curvature delineates the the upthrown edge of the footwall adjacent to the faults (the green arrows in Figure 5c) rather than the fault discontinuity itself. In addition, the most-positive curvature delineates the anticlinal components of flexures and folds, including the axes of the pop-up blocks identified with yellow arrows in Figure 5c.

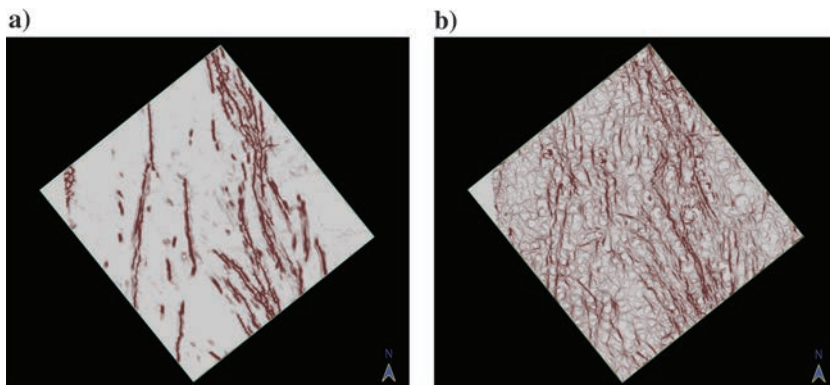


Figure 13. Time slices at $t = 1300$ ms through the fault probability volumes computed from the (a) coherence attribute and (b) short wavelength most-positive curvature. Notice the difference in the level of detail in the two displays (data courtesy of Arcis Seismic Solutions, TGS, Calgary).

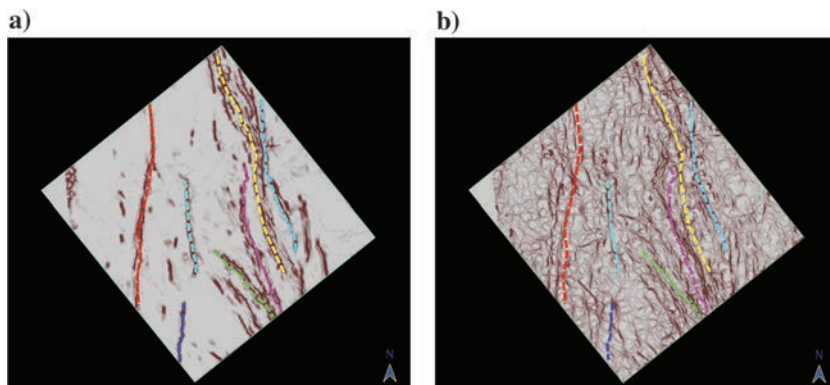


Figure 14. Time slices at $t = 1300$ ms through the fault probability volumes computed from the (a) coherence and (b) short wavelength most-positive curvature. Some of the lineaments as seen on the fault probability display in panel (a) are tracked using different colors and then copied on to the display in panel (b). Notice that many of the lineaments seen on the display in panel (b) do not exactly match the tracked lineaments, and in fact, they are shifted toward the footwall side of the normal faults as seen in Figure 1a (data courtesy of Arcis Seismic Solutions, TGS, Calgary).

not difficult to follow the difference pointed above. Whereas a sharp lineament on a vertical seismic section coming from a normal fault exactly coincides with the coherence lineament, the most-positive curvature lineament is slightly displaced to one side because it comes from the upthrown side of the fault, and the negative curvature lineament is slightly displaced to the other side because it comes from the downthrown side of the fault. Additional positive and negative curvature lineaments correspond to anticlines, synclines, and relay ramps in the data, as well as to smaller faults that fall below seismic resolution. All these curvature signatures will yield noticeable probability measures on the fault probability displays, and they should be judiciously considered in the interpretation.

Conclusion

The volumetric fault image enhancement workflow described above provides a means of comparing the fault dip magnitude, fault dip azimuth, and fault probability attributes for linear discontinuities. This approach helps in the manual interpretation of faults on workstations, and it provides a useful input for software designed for automatic extraction of fault planes. The methodology followed in this work enhances the desired orientation of linear geologic features, and their interpretations can be carried forward to the next step in terms of their correlations with production data.

Acknowledgment

We wish to thank Arcis Seismic Solutions, TGS, Calgary, for permission to present this work.

References

- AlBinHassan, N. M., Y. Luo, and M. N. Al-Faraj, 2006, 3D edge-preserving smoothing and applications: *Geophysics*, **71**, no. 4, P5–P11, doi: [10.1190/1.2213050](https://doi.org/10.1190/1.2213050).
- Al-Dossary, S., and K. J. Marfurt, 2006, 3-D volumetric multispectral estimates of reflector curvature and rotation: *Geophysics*, **71**, no. 5, P41–P51, doi: [10.1190/1.2242449](https://doi.org/10.1190/1.2242449).
- Bahorich, M., and S. Farmer, 1995, The coherence cube: *The Leading Edge*, **14**, 1053–1058, doi: [10.1190/1.1437077](https://doi.org/10.1190/1.1437077).
- Bakker, P., 2003, Image structure analysis for seismic interpretation: Ph.D. thesis, Technische Universiteit Delft.
- Barnes, A. E., 2006, A filter to improve seismic discontinuity data for fault interpretation: *Geophysics*, **71**, no. 3, P1–P4, doi: [10.1190/1.2195988](https://doi.org/10.1190/1.2195988).
- Chopra, S., and K. J. Marfurt, 2007, 3D seismic attributes for reservoir characterization and prospect mapping: SEG.
- Chopra, S., and K. J. Marfurt, 2008, Gleaning meaningful information from seismic attributes: *First Break*, **26**, 43–53, doi: [10.3997/1365-2397.2008012](https://doi.org/10.3997/1365-2397.2008012).
- Chopra, S., and K. J. Marfurt, 2010, Integration of coherence and volumetric curvature images: *The Leading Edge*, **29**, 1092–1107, doi: [10.1190/1.3485770](https://doi.org/10.1190/1.3485770).

- Chopra, S., and K. J. Marfurt, 2013, Preconditioning seismic data with 5D interpolation for computing geometric attributes: *The Leading Edge*, **32**, 1456–1460, doi: [10.1190/1.1444456](https://doi.org/10.1190/1.1444456).
- Dorn, G., and B. Kadlec, 2011, Automatic extraction in hard and soft-rock environments: 31st Annual Bob, F. Perkins Research Conference on Seismic attributes — New views on seismic imaging: Their use in exploration and production, 587–619.
- Gersztenkorn, A., and K. J. Marfurt, 1999, Eigenstructure-based coherence computations as an aid to 3D structural and stratigraphic mapping: *Geophysics*, **64**, 1468–1479, doi: [10.1190/1.1444651](https://doi.org/10.1190/1.1444651).
- Hoecker, C., and G. Fehmers, 2002, Fast structural interpretation with structure-oriented filtering: *The Leading Edge*, **21**, 238–243, doi: [10.1190/1.1463775](https://doi.org/10.1190/1.1463775).
- Hutchison, B., 2016, Application and limitation of seismic attributes on 2D reconnaissance surveys: M.S. thesis, The University of Oklahoma.
- Kuwahara, M., K. Hachimura, S. Eiho, and M. Kinoshita, 1976, Digital processing of biomedical images: Plenum Press.
- Lavialle, O., S. Pop, C. Germain, M. Donias, S. Guillon, and N. Keskes, 2007, Seismic fault preserving diffusion: *Journal of Applied Geophysics*, **61**, 132–141, doi: [10.1016/j.jappgeo.2006.06.002](https://doi.org/10.1016/j.jappgeo.2006.06.002).
- Luo, Y., S. Al-Dossary, and M. Alfaraj, 2002, Edge-preserving smoothing and application: *The Leading Edge*, **21**, 136–158, doi: [10.1190/1.1452603](https://doi.org/10.1190/1.1452603).
- Machado, G., A. Alali, B. Hutchinson, O. Olorunsola, and K. J. Marfurt, 2016, Display and enhancement of volumetric fault images: *Interpretation*, **4**, no. 1, SB51–SB61, doi: [10.1190/INT-2015-0104.1](https://doi.org/10.1190/INT-2015-0104.1).
- Marfurt, K. J., 2006, Robust estimates of reflector dip and azimuth: *Geophysics*, **71**, no. 4, P29–P40, doi: [10.1190/1.2213049](https://doi.org/10.1190/1.2213049).
- Marfurt, K. J., R. L. Kirlin, S. H. Farmer, and M. S. Bahorich, 1998, 3-D seismic attributes using a running window semblance-based algorithm: *Geophysics*, **63**, 1150–1165, doi: [10.1190/1.1444415](https://doi.org/10.1190/1.1444415).



Satinder Chopra has 33 years of experience as a geophysicist specializing in processing, reprocessing, special processing, and interactive interpretation of seismic data. He has rich experience in processing various types of data such as VSP, well-log data, and seismic data. He has been the 2010/11 CSEG distinguished lecturer, the 2011/12 AAPG/SEG distinguished lecturer, and the 2014/15 EAGE e-distinguished lecturer. He has published eight books and more than 380 papers and abstracts. His work and presentations have won several awards, the most notable ones being the CSEG Honorary Membership (2014) and Meritorious Service (2005) Awards, 2014 Association of Professional Engineers, Geologists and Geophysicists of Alberta (APEGA) Frank Spragins Award, the

2010 AAPG George Matson Award, the 2013 AAPG Jules Braunstein Award, SEG Best Poster Awards (2007, 2014), and CSEG Best Luncheon Talk (2007). He is a member of SEG, CSEG, CSPG, EAGE, AAPG, and APEGA. His research interests focus on techniques surrounding the characterization of reservoirs.



Kurt J. Marfurt began his geophysical career teaching geophysics and contributing to an industry-supported consortium on migration, inversion, and scattering (project MIDAS) at Columbia University's Henry Krumb School of Mines in New York City. In 1981, he joined Amoco's Tulsa Research Center and spent the next

18 years doing or leading research efforts in modeling, migration, signal analysis, basin analysis, seismic attribute analysis, reflection tomography, seismic inversion, and multicomponent data analysis. In 1999, he joined the University of Houston as a professor in the Department of Geosciences and as a director of the Allied Geophysics Laboratories. He is a member of the Geophysical Societies of Tulsa and Houston, SEG, EAGE, AAPG, AGU, and SIAM, and he serves as an assistant editor for *GEOPHYSICS*. His current research activity includes prestack imaging, velocity analysis and inversion of converted waves, computer-assisted pattern recognition of geologic features on 3D seismic data, and interpreter-driven seismic processing. His research interests include seismic signal analysis, 3D seismic attributes, seismic velocity analysis, subsurface imaging, and multicomponent data analysis.